Phenethylammonium Functionalization Enhances Near-Surface Carrier Diffusion in Hybrid Perovskites

Ti Wang,[1,2#] Yongping Fu,[3#] Linrui Jin,[1#] Shibin Deng,[1] Dongxu Pan,[3] Liang Dong,[2] Song Jin,[3*] and Libai Huang[1*]

[1] Department of Chemistry, Purdue University, West Lafayette, IN 47907, USA

[2] School of Physics and Technology and Key Laboratory of Artificial Micro- and Nano-structures of Ministry of Education, Wuhan University, Wuhan 430072, China

[3] Department of Chemistry, University of Wisconsin-Madison, Madison, WI 53706, USA

* Correspondence to: libai-huang@purdue.edu, jin@chem.wisc.edu
# These authors contributed equally to this work

Abstract

Understanding semiconductor surface properties and manipulating them chemically are critical for improving their performance in optoelectronic devices. Hybrid halide perovskites have emerged as an exciting class of highly efficient solar materials; however, their device performance could be limited by undesirable surface properties that impede carrier transport and induce recombination. Here we show that surface functionalization of methylammonium lead iodide ($MAPbI_3$) perovskite with phenethylammonium iodide (PEAI), a commonly employed spacer cation in two-dimensional perovskites, can enhance carrier diffusion in the near-surface regions and reduce defect density by more than one order of magnitude. Using transient transmission and reflection microscopy, we selectively imaged the transport of the carriers near the (001) surface and the bulk carriers in single-crystal $MAPbI_3$ microplates. The surface functionalization increases the diffusion coefficient of the carriers in a 40-nm subsurface region from ~ 0.6 cm^2s^{-1} to ~ 1 cm^2s^{-1}, similar to the value for bulk carriers. These results suggest the PEA ligands are effective in suppressing surface defect and phonon scattering and shed light on the mechanisms for enhancing photophysical properties and improving solar cell efficiency.

TOC Graphic

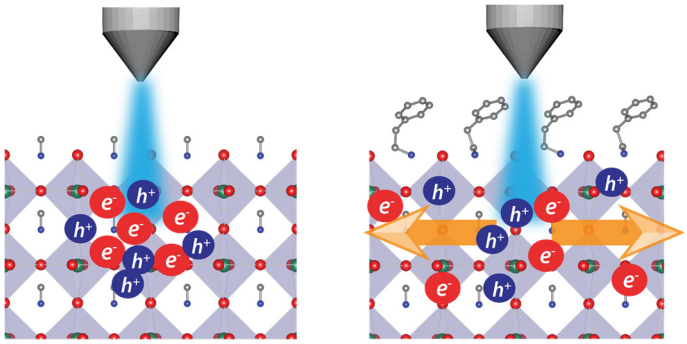

Organic-inorganic hybrid lead halide perovskites have emerged as an exciting class of optoelectronic materials that have been successfully demonstrated in highly efficient solar cells, light-emitting devices, lasers and photodetectors.[1-8] Managing surface-related carrier scattering and recombination processes are critical for achieving high performance optoelectronic devices. For conventional semiconductors (e.g. elemental and III-V), surface functionalization can be achieved by forming covalent bonds with the surface atoms, which renders the surfaces more electronically benign to reduce recombination and scattering.[9-11] However, the chemical bonding in hybrid perovskites is ionic and the surface defect levels are generally much lower than those found in conventional covalent semiconductors. Therefore these structures require different surface functionalization approaches from those designed for the dangling bonds on the surfaces of covalent semiconductors,[8,12] Recently, several surface functionalization strategies have been successfully applied to hybrid perovskites and led to improved light emitting diode efficiency, solar cell efficiency and stability.[13-18] Binding of small molecules on the surfaces, such as Lewis bases and acids and molecules with N-H and carbonyl groups, has been found to be effective in passivating the organic cation or halide vacancies.[13-17]

However, thus far, the photophysical investigation on the effects of surface functionalization has been largely focused on carrier recombination over the nanosecond or longer timescale,[19-23] much less is known about the effects on carrier transport near the surfaces. At the microscopic level, the transport of charge carriers is limited by scattering of phonons, defects and impurities, and these scattering processes can be modified significantly at or near the surfaces. These scattering processes alter the momentum of the carriers on femtosecond timescale and the higher frequency of these events leads to slower carrier diffusion near the surfaces,[24] which has been observed in conventional semiconductors such as Si and GaAs.[25-27] The impeded transport of

near-surface carriers could deteriorate the performance of solar cells and photodetectors. A viable approach to reduce scattering and enhance near-surface carrier transport in 3D perovskites is to draw inspiration from two-dimensional (2D) Ruddlesden–Popper (RP) phase perovskites. By inserting large long-chain ammonium (LA) cations, the 3D metal-halide frameworks can be sliced to form 2D layered perovskites.[28-30] Notably, the LA spacer cations of 2D perovskites have been demonstrated to passivate defects, increase structural rigidity, and modify electron-phonon coupling,[31-34] which suggests their potentials in reducing phonon and defect scattering at the surface of 3D hybrid perovskites. Specifically, it has been reported recently that treating thin films of polycrystalline perovskites with phenethylammonium iodide (PEAI) can improve the efficiency and stability of solar cells.[35,36] However, the focus thus far has been on the ligands' impact on carrier recombination and their effect on carrier diffusion has not been explored in 3D hybrid perovskites.

Here we show using PEA surface functionalization can improve the near-surface carrier transport in methylammonium lead iodide ($MAPbI_3$) using single-crystal microplate samples. These well-faceted microplates, which have lateral sizes of more than 10 microns and thickness less than a micron, serve as ideal model systems for physical studies for solar cell devices.[5,37-39] To differentiate the carrier transport in the near-surface regions from the bulk, we employed femtosecond transient transmission and reflection microscopy capable of directly visualizing carrier diffusion with nanoscale spatial resolution.[40] The measurements on single-crystals allow for the elucidation of facet-specific surface effects without being confounding by those from the grain boundaries, which distinguishes this study from the previous spectroscopic studies on polycrystalline thin films.[41-44] These results show that the PEA functionalization reduces surface defect density by one order of magnitude and significantly suppresses carrier scattering. With the

PEA surface ligands, carrier transport behaviors in the near-surface (25-40 nm) region are similar to those in the bulk. In contrast, diffusion constant for the carriers in the subsurface region is only about half of the bulk carriers for the untreated reference samples. We attribute this increased diffusion to the reduced carrier scattering and trap states at the PEA-terminated surface.

Results and Discussion

Sample preparation and surface characterizations. Reference $MAPbI_3$ microplates were synthesized by following methods published previously.[5,37] Each individual microplate is a single crystal with well-controlled facets and known chemical compositions, allowing for systematic investigation of the impact of surface functionalization on carrier dynamics and transport. Transmission electron microscopy (TEM) confirmed the exposing facets were (001) or (110) planes of tetragonal $MAPbI_3$ phase (which are equivalent to the (001) plane of the pseudo-cubic lattice).[5] As these microplates were grown under an iodide-rich environment, the surfaces were terminated by MAI (illustrated in Figure 1a), as supported by scanning tunneling microscopy measurements and photoemission spectroscopy studies on single crystals.[45-48] Under-coordinated Pb atoms are unlikely to be present at the surface, because the excess iodide anion in the growth solution should facilitate the formation of coordinative Pb−I bonds. When all PbI_6 octahedra are complete, the $MAPbI_3$ surface must be terminated by the MA^+ cations in the cuboctahedral voids to balance the charges.

We choose PEA as the surface ligands based on previous reports that show incorporating the PEA spacer cation in the 2D perovskites reduces structural disorder and enhances exciton diffusion.[31,32,34,49,50] Surface-functionalized single-crystal $MAPbI_3$ microplates (illustrated in Figure 1b) were synthesized by immersing a glass slide coated with a lead acetate thin film into an isopropanol solution containing both PEAI and MAI (see more details in Materials and

Methods).[51] When PEA and MA cations coexist in the growth solution, it is thermodynamically more favorable for PEA to occupy the surface sites, due to the additional energy gained from van der Waals interactions between adjacent PEA cations.[51] It is noted that the surface bound cations are in dynamic equilibrium with the free cations in the solution. The key to grow surface-functionalized $MAPbI_3$ microplates is to control the concentration ratio of PEAI to MAI (α) to around 0.52 (Figures S1 and S2), so that it is high enough for PEA cations to functionalize the 3D perovskite surface with high coverage, as supported by the previous report on stabilizing the metastable formamidinium lead iodide perovskite phase using surface functionalization with PEA;[51] but still low to minimize the formation of various 2D RP phase perovskites of $(PEA)_2(MA)_{n-1}Pb_nI_{3n+1}$ (n is an integer).[52] If the α value was increased slightly to ~ 0.64, we found the growth of 3D $MAPbI_3$ microplates with surface PEA ligands is kinetically favored even though the formation of 2D RP perovskites is thermodynamically favored (Figures S3-S5). Compared to the reference $MAPbI_3$ microplates grown without PEAI, the presence of PEA cations in the growth solution clearly promotes anisotropic growth of the resulting single crystals (see optical and scanning electron microscope images in Figure S6). This phenomenon is similar to surfactant-induced anisotropic growth in semiconductor nanocrystals,[53] suggesting that the surface of the perovskites is capped by PEA cations. The time dependent PXRD collected on the nanostructure films at $\alpha = 0.52$ show that the initial formed products were 3D perovskites (Figure S7). With these results, a rough growth "phase diagram" as a function of α value and reaction time is illustrated in Figure S8. Please also see additional discussion on the crystal growth process in the Supporting Information.

The optical image of the as-grown PEA-terminated $MAPbI_3$ sample (Figure 1c, SEM images shown in Figure S6b) reveals rectangular microplates with a length of more than 10 micron in one

dimension as well as nanowires. Figure 1d shows a low-resolution TEM image of a representative PEA-terminated $MAPbI_3$ microplate. The corresponding selected-area electron diffraction (SAED) pattern (Figure 1e) shows a set of sharp diffraction spots that can be indexed to a pseudo-cubic $MAPbI_3$ structure with a zone axis of [001], which unambiguously confirmed the 3D perovskite phase and revealed the top surface facet of (001).

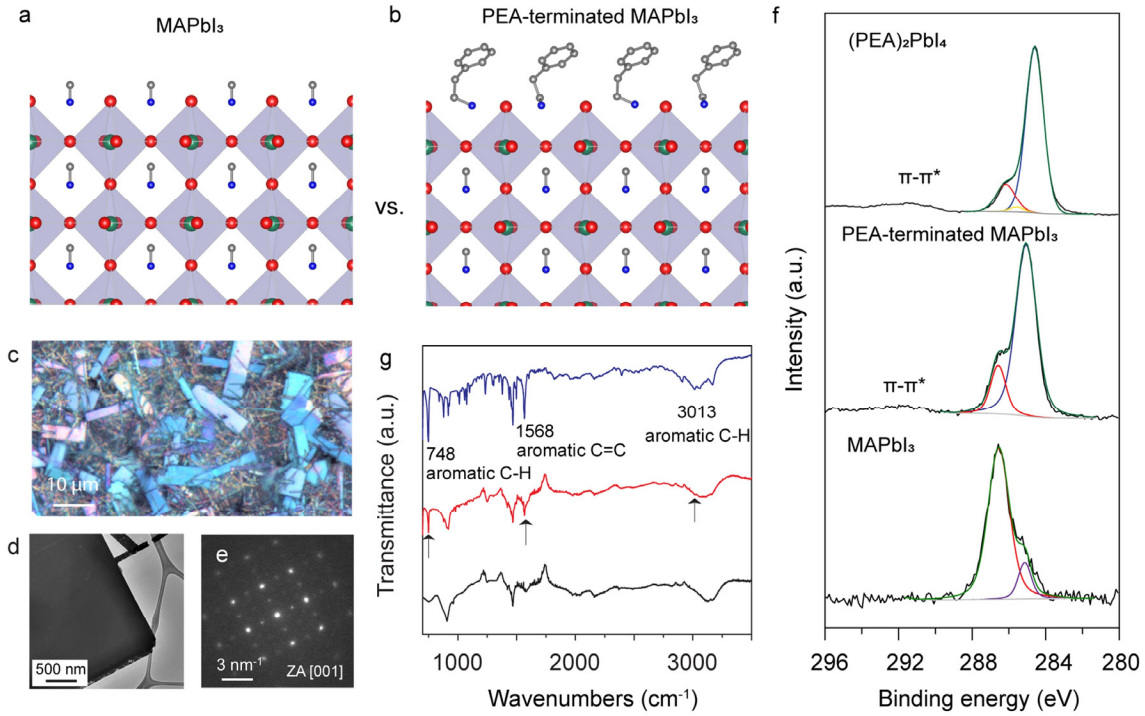

Figure 1. Surface chemistry and structural characterizations of reference $MAPbI_3$ and PEA-terminated $MAPbI_3$ microplates. (a-b) Schematic illustrations of the (001) surface of $MAPbI_3$ terminated by MA (a) and PEA (b) cations, respectively. (c) Optical image of a PEA-terminated $MAPbI_3$ sample that contains both microplates and nanowires. (d) Low-resolution TEM images of a PEA-terminated $MAPbI_3$ microplate and (e) the corresponding SAED pattern along the [001] zone axis (ZA) of the tetragonal phase. (f) Fitted high-resolution XPS of C 1s region for PEA-terminated $MAPbI_3$, in comparison with the XPS spectra for $MAPbI_3$ and $(PEA)_2PbI_4$. (g) FTIR spectra of PEA-terminated $MAPbI_3$ (red), reference $MAPbI_3$ (black) and $(PEA)_2PbI_4$ (blue) 2D perovskites.

To confirm the presence of PEA cations on the surfaces of treated microplates, we performed surface-sensitive X-ray photoelectron spectroscopy (XPS) on the functionalized sample and two control samples, i.e. $MAPbI_3$ and $(PEA)_2PbI_4$ (Figure 1f). The C 1s XPS spectrum of $MAPbI_3$ shows a major peak at 286.6 eV, which is assigned to the C atoms in the MA cations. Note the

small shoulder located at 285.1 eV may be from adventitious carbon or other contamination. The spectrum of $(PEA)_2PbI_4$ shows a major peak at 284.6 eV from the aromatic C (sp^2) atoms in the benzene ring, a shoulder peak (on the left side) from the C (sp^3) atoms in the ethylammonium group, and a π-π* satellite at several eV higher binding energy of the main peak. The PEA-terminated $MAPbI_3$ shows mostly similar spectral profile to the $(PEA)_2PbI_4$. The major peak can be assigned to the aromatic C atoms in the PEA cations, whereas the shoulder peak with a slightly higher peak height can be assigned to the combination of sp^3 C atoms in the PEA cations and C atoms in the MA cations. Moreover, the π-π* satellite was clearly observed for both $(PEA)_2PbI_4$ and PEA-terminated $MAPbI_3$ samples but not present in $MAPbI_3$ sample. These results confirm the surface termination by PEA cations in the functionalized crystals. Fourier transform infrared (FTIR) spectroscopy measurements on these three samples were also conducted (Figure 1g). Peaks corresponding to aromatic C−H and aromatic C=C vibrational modes at 748 cm^{-1} and 1568 cm^{-1}, respectively, were clearly observed for the PEA-terminated $MAPbI_3$. These peaks were also observed in the $(PEA)_2PbI_4$, but were absent from the reference $MAPbI_3$.

Surface carrier recombination. We first employed steady-state and time-resolved optical spectroscopy to investigate how the surface functionalization influences carrier recombination. As shown by the photoluminescence (PL, Figure 2a) and absorption (Figure S9) spectra, the optical bandgap is not affected significantly by the surface PEA cations. The representative PL spectrum of a PEA-terminated $MAPbI_3$ microplate exhibits a single band-edge emission peak of 782 nm with a full-width at half-maximum (FWHM) of 50 nm, which is almost identical to the reference $MAPbI_3$ microplate (Figure 2a). Statistical analysis of the emission spectra from more than 10 functionalized and control $MAPbI_3$ microplates reveals no systematic difference in the PL peak energy and peak width (inset of Figure 2a). These results confirm the absence of low *n*-value 2D

RP perovskites (i.e. *n* is less than 7), whose PL emission peaks are distinct from the 3D $MAPbI_3$.[29] It has been predicted that 2D RP perovskites with *n* value greater than 20 would behave like 3D perovskite.[54] It may be possible that some large *n*-value 2D RP perovskites (i.e. *n* is larger than 7) form along with the 3D structure in the functionalized microplates. Nevertheless, if the *n* values are large enough, the 2D RP perovskites can be thought as surface-functionalized 3D perovskite nanostructures.

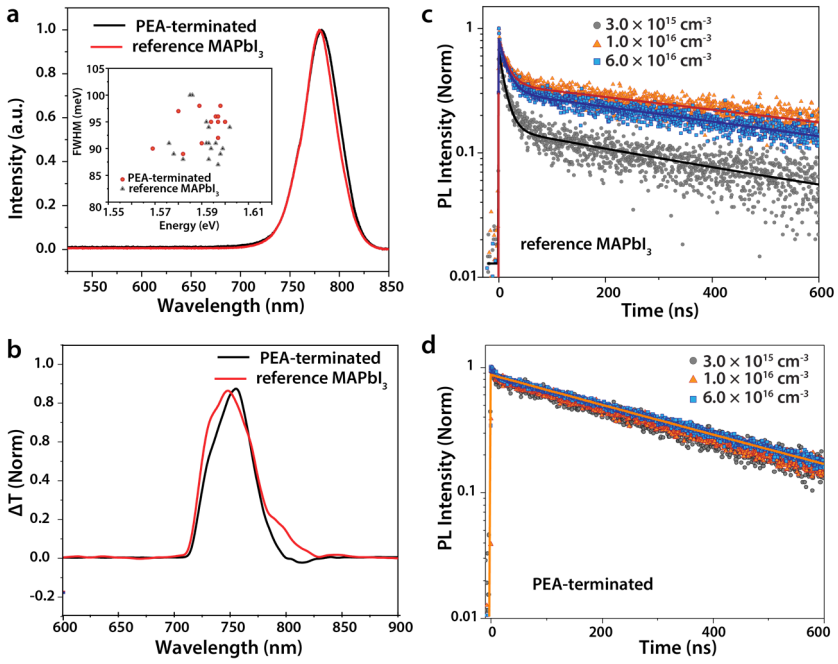

Figure 2. Carrier recombination in functionalized $MAPbI_3$ microplates in comparison with reference $MAPbI_3$ microplates. (a) Confocal PL spectra of an individual functionalized $MAPbI_3$ microplate in comparison with the reference $MAPbI_3$ microplate. Inset: statistical analysis of the PL peak energy and FWHM of the confocal PL spectra collected on PEA-terminated and reference $MAPbI_3$ microplates. (b) Broadband TA spectra at zero delay time for a surface-functionalized and a reference $MAPbI_3$ microplate with a pump energy of 1.77 eV. Carrier–density dependent time-resolved PL dynamics of the reference (c) and PEA-terminated $MAPbI_3$ microplates (d). The solid lines are bi-exponential fits (reference $MAPbI_3$) and single-exponential fits (PEA-terminated $MAPbI_3$) convoluted with the instrument response function, and the fitting parameters are given in Table S1. The PL lifetime measurements were carried out in reflection mode with a 2.80 eV excitation, exciting carriers within 50-nm of depth from the surface.

Figure 2b compares the broadband transient absorption (TA) spectra of a functionalized $MAPbI_3$ microplate vs. a reference $MAPbI_3$ microplate at zero time-delay. Upon photoexcitation,

a ground state bleach band (positive signal in $\Delta T/T$, and ΔT is pump-induced change in probe transmission T) centered around the bandgap at 1.64 eV (756 nm) is observed due to band-filling effect. Photo-induced bleach below the bandgap was observed for the untreated microplate, which is likely due to the sub-bandgap defect states.[43] The TA spectra also confirm the phase purity of the samples. If the structures were 2D/3D heterostructures, one would expect higher-energy exciton bleach bands due to the 2D perovskites.[55]

Comparative PL lifetime measurements show the PEA surface functionalization significantly reduced the carrier recombination rate. The PL lifetime measurements were carried out in reflection mode with a 2.80 eV excitation with a penetration depth of 50 nm as calculated by $1/a$ (a is absorption coefficient).[22] As shown in Figure 2c, carrier dynamics in an untreated reference $MAPbI_3$ microplate exhibits a bi-exponential decay, with a fast component of 10-15 ns and a slow component of 500-800 ns (fitting parameters are listed in Table S1). The dynamics also exhibits a non-monotonous dependence on carrier density, which can be explained by the combined effects of defect trapping and bi-molecular recombination as schematically illustrated in Figure S10 and described in the SI.[56] Briefly, as the carrier density increases from 3.0×10^{15} cm^{-3} to 1.0×10^{16} cm^{-3}, the recombination dynamics becomes slower with reduced contribution from the fast component, which can be attributed to the filling of the trap states by the photoexcited carriers. When the carrier density is further increased to 6.0×10^{16} cm^{-3}, the dynamics becomes faster due to higher bimolecular recombination rate.

Significantly, the fast nanosecond decay component in the PL decay is mostly eliminated by the PEA functionalization (Figure 2d) and the carrier recombination exhibits largely single-exponential decay behavior, with a lifetime of ~ 350 ns. As previously suggested, carrier recombination at the top and bottom surfaces limits the carrier lifetimes in thin films of

$MAPbI_3$.[21,22] The suppression of the fast recombination pathway (~ 10 ns) suggests that surface defect density is reduced by PEA functionalization. Moreover, the recombination dynamics for the PEA-terminated microplate shows negligible dependence on the carrier density ranging from 3.0 × 10^{15} cm^{-3} to 1.0 × 10^{16} cm^{-3}, suggesting a defect density below 3.0 × 10^{15} cm^{-3}. The carrier density-dependent PL decay dynamics in Figures 2c and 2d were modeled to extract the defect density by iteratively fitting to the trap-mediated recombination model[56] (Figures S11 and S12, Table S2). The defect density in the reference $MAPbI_3$ is estimated to be ~ 7 × 10^{15} cm^{-3} and it is reduced by one order of magnitude to ~ 5 × 10^{14} cm^{-3} by PEA surface functionalization.

We rule out that the fast decay in the reference crystals is due to carrier diffusion out of the excitation area. First, the collection of emission is in wide-field mode where all the emission is collected and diffusion in lateral or vertical dimension should contribute negligibly to the PL dynamics. Further, the fast decay component was only observed in the reference crystals, not the PEA-terminated crystals that have larger surface lateral diffusion constants as discussed below, which again suggests that the fast decay component is not due to diffusion, but the carrier trapping process.

Bulk and near-Surface carrier transport imaged by transient absorption microscopy. The transport of carriers in the near-surface region can differ significantly from the bulk due to surface and defect scattering.[25-27] To investigate how the surface functionalization with PEA cations affects carrier transport, we further employed ultrafast microscopy[40] to directly image carrier transport in single microplates. We have demonstrated transient absorption microscopy (TAM) as a useful tool to visualize carrier migration with a high time resolution and spatial precision.[40,57] Here we employed TAM in both transmission and reflection mode and we first discuss the results from the transmission mode. By taking advantage of strongly wavelength-dependent absorption

coefficient of halide perovskite materials,[22] carrier transport in the near surface region and the bulk can be selectively imaged (Figure 3a). The penetration depths of 3.10 and 1.77 eV pump photons are estimated to be 40 and 500 nm as illustrated in Figure 3b based on the absorption of $MAPbI_3$ (Figure S9).[22] Most carriers are generated within the topmost 40 nm from the surface by using a 3.10 eV pump phonon energy (Figure 3b). In contrast, more or less the entire depth of the microplate with a thickness of 400 nm can be excited with 1.77 eV pump photon energy (Figure 3b).

To image carrier transport, the pump beam was held at a fixed position while the probe beam was scanned relative to the pump with a Galvanometer scanner (more details in Methods and Figure S13). A probe energy of 1.64 eV (756 nm) resonant with the ground state bleach band is employed to image the population of cooled carriers at the bandgap. The initial carrier profile visualized in Figure 3b is given by $n(x,y,z,0) = N_0 exp\,(-\alpha z) exp[-\frac{(x-x_0)^2}{2\sigma_{x,0}^2} - \frac{(y-y_0)^2}{2\sigma_{y,0}^2}]$, as created by a Gaussian pump beam with variances of $\sigma_{x,0}^2$ and $\sigma_{y,0}^2$ at position (x_0, y_0) and a pulse duration of ~ 300 fs. The initial population decays exponentially in the z direction. In the transmission mode, ΔT is integrated over the z direction and the lateral carrier transport in the xy plane was visualized by 2D TAM images at different delay times (Figures 3c-3f). At a later delay time t, the carrier density also follows a Gaussian distribution as given by, $n(x,y,t) = N_t exp[-\frac{(x-x_0)^2}{2\sigma_{x,t}^2} - \frac{(y-y_0)^2}{2\sigma_{y,t}^2}]$. The TAM images in Figures 3c-3f are thus fitted by 2D Gaussian functions with variances of $\sigma_{x,t}^2$ and $\sigma_{y,t}^2$. Because carrier transport is isotropic in the xy plane, one-dimensional scanning $n(x,0,t)$ instead of two-dimensional imaging $n(x,y,t)$ was performed for the following TAM measurements to reduce the data redundancy and $\sigma_t^2 = \sigma_{x,t}^2 = \sigma_{y,t}^2$. The one-dimensional

population profiles for a reference and a PEA-terminated microplate are shown in Figures 4a, b and 4c, d, respectively.

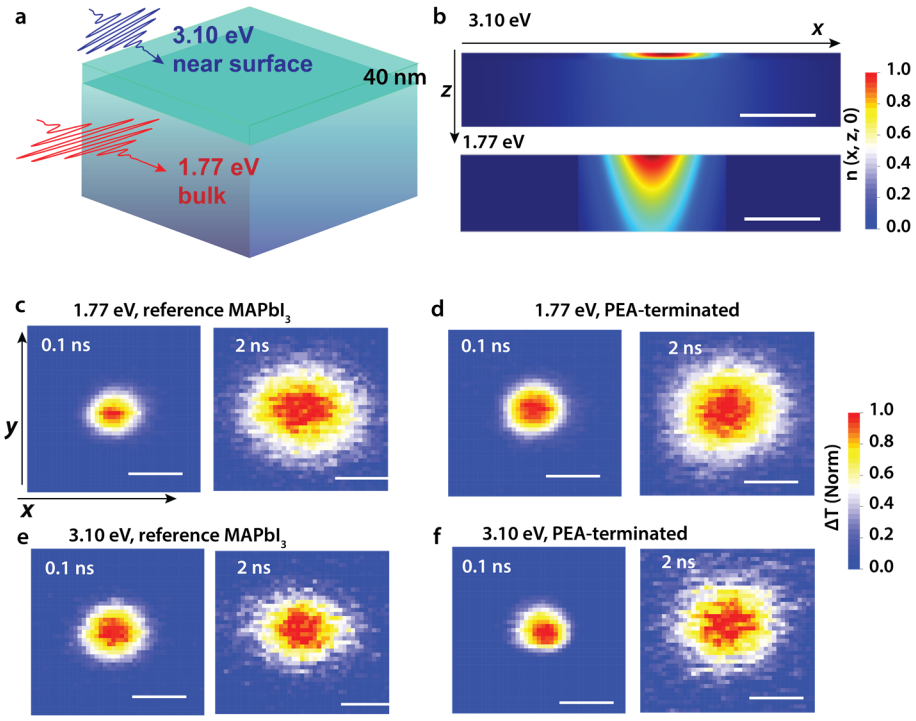

Figure 3. **Transient transmission microscopy imaging of near-surface and bulk carrier diffusion.** (a) Schematic illustration of selectively excitation of carriers in the near-surface regions. With 3.10 eV pump energy, only carriers within 40-nm distance of the sample surface was excited. The whole microplate can be excited with 1.77 eV pump energy. (b) Calculated depth-dependent carrier population generated by 3.10 eV and 1.77 eV pump at time zero. Scale bar: 400 nm. (c-f): The TAM images of the carrier transport at various delay times with a pump photon energy of 1.77 eV for a reference $MAPbI_3$ microplate (c) and a PEA-terminated microplate (d). The TAM images of the carrier transport at various delay times with a pump photon energy of 3.10 eV for a reference $MAPbI_3$ microplate (e) and a PEA-terminated microplate (f). Probe energy = 1.64 eV. Color scale represents the intensity of pump-induced differential transmission (ΔT) of the probe and every image has been normalized by the peak value. Scale bar: 1 μm.

The effective diffusion constant D can be extracted by the broadening of the Gaussian variances, $D = \frac{\sigma_{t2}^2 - \sigma_{t1}^2}{2(t_2 - t_1)}$,[40] and the D measured in the transmission mode corresponds to an averaged value over z. The carrier diffusion over the z direction will be discussed by comparing to the results from the reflection mode in the next section. Both electrons and holes should contribute more or less equally to the transport due to their similar effective masses.[58] To avoid complications

from hot phonon effects, the carrier density for all measurements was kept around 5×10^{17} cm^{-3}, below the threshold for phonon bottleneck.[14,59-61] We have also confirmed that higher-order processes such as Auger recombination are negligible at a carrier density of ~ 5×10^{17} cm^{-3} (Figure S14). All the measurements were performed in the linear regime so that the TA signal was proportional to carrier density.

Carrier transport in an untreated reference $MAPbI_3$ microplate is shown in Figures 3c and 3e for pump photon energies of 1.77 eV and 3.10 eV, respectively. We note that the 3.10 eV pump creates hot carriers with excess kinetic energy and enhanced transport at timescale < 100 ps,[57] which leads to a larger $\sigma^2_{100\,ps}$ than the 1.77 eV pump. To eliminate the complications from hot carriers, here we focus on the transport of cooled carriers in thermal equilibrium with the lattice on timescale greater than 100 ps. The overall distance of carrier transport is shorter with a 3.10 eV pump, indicating that carrier diffusion is impeded in the near-surface region compared to the bulk. In comparison, the TAM images for a PEA functionalized microplate are shown in Figures 3d (1.77 eV) and 3f (3.10 eV), exhibiting similar carrier transport behaviors for the near-surface carriers as those of the bulk carriers.

Figures 4e and 4f show that σ_t^2 grows linearly as a function of delay time for $t > 100\,ps$, which is expected for a diffusive transport of the thermally equilibrated cooled carriers. We extracted *D* with a 1.77 eV pump to be 1.13 ± 0.01 cm^2s^{-1} for the bulk carriers in the reference microplate. In comparison, an effective *D* of 0.50 ± 0.01 cm^2s^{-1} was obtained for the near-surface carriers of the same microplate excited by a 3.10 eV pump, which is only 45% of the bulk diffusion coefficient (Figure 4e). With a pump photon energy of 2.25 eV and a penetration depth of about 180 nm, the diffusion coefficient was found to have a value of 0.97 ± 0.02 cm^2s^{-1} (Figure S15), closer to the bulk-like carrier diffusion coefficient. The reduced carrier diffusion constant in the

near surface region is likely due to increased carrier trapping and scattering. For instance, the effective diffusion constant near the surfaces is more than three orders of magnitude smaller than in the bulk for GaAs.[27] For the PEA-terminated $MAPbI_3$ microplate shown in Figures 4c, 4d and 4f, the bulk carriers have a D of 1.03 ± 0.01 cm^2s^{-1}, similar to that of the reference sample, which confirms that the carrier transport properties of the bulk do not change significantly upon surface functionalization. However, with a pump photon energy of 3.10 eV, D is measured to be 1.05 ± 0.01 cm^2s^{-1} for the near-surface carriers in the same microplate (Figure 4f), which indicates that the carrier diffusion constant in the near-surface region is fully restored to the bulk value by the surface functionalization with PEA cations.

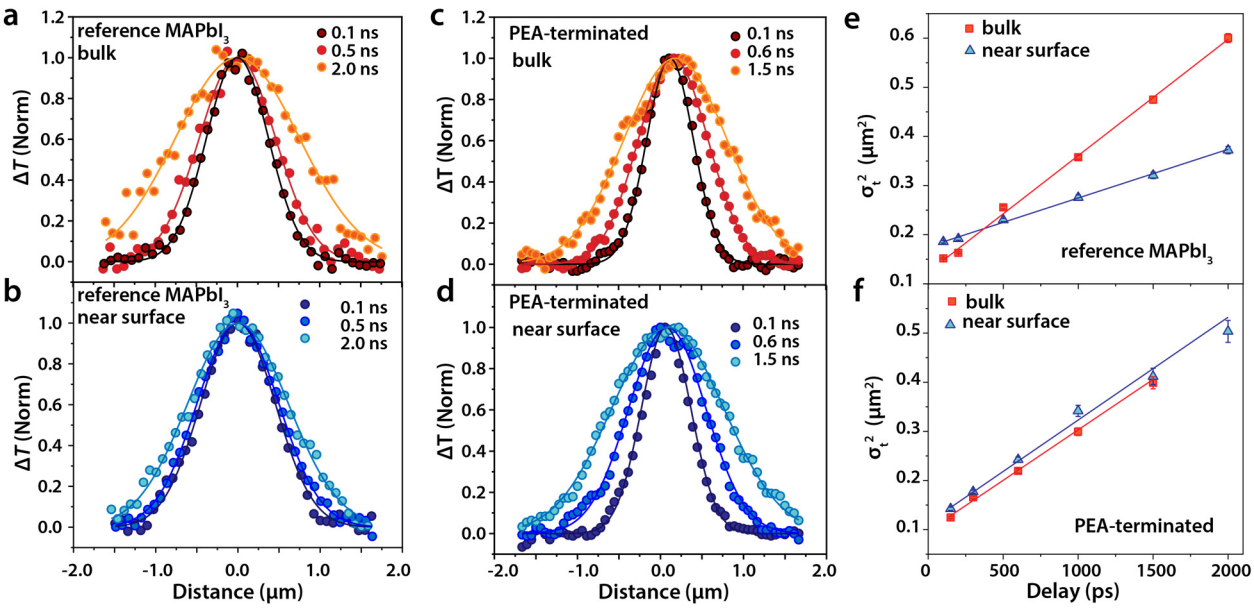

Figure 4. **Near-surface and bulk carrier diffusion in reference and PEA-terminated $MAPbI_3$ microplates.** (a-d) 1D carrier population profiles fitted with Gaussian functions at different delay times, with the maximum ΔT signal normalized. Bulk carriers (a) and near-surface carriers (b) in a reference $MAPbI_3$ microplate. Bulk carriers (c) and near-surface carriers (d) in a PEA-terminated $MAPbI_3$ microplate. (e) σ_t^2 plotted as a function of pump-probe delay time in the reference $MAPbI_3$ microplate extracted from the data shown in (a) and (b). Solid lines are the linear fitting to calculate the diffusion constants. (f) σ_t^2 plotted as a function of pump-probe delay time in the PEA-terminated $MAPbI_3$ microplate extracted from the data shown in (c) and (d). Solid lines are the linear fitting to calculate the diffusion constants.

Reflection-mode TAM measurements and diffusion in *z*. To investigate the effect of carrier diffusion in the *z* direction, we also imaged the near-surface carrier transport using transient reflection microscopy. In the reflection mode, the effective probing depth is ~$\lambda/4\pi n$, where λ is the probe wavelength and n is the reflective index at the probe wavelength.[26,62] We used a pump wavelength of 700 nm (1.77 eV) to excite the entire depth of the microplates and a probe wavelength at 780 nm corresponding to a probing depth of ~ 25 nm. The pump-induced change in the probe reflection (ΔR) is imaged as a function of probe position. In such a way, the ΔR measured comes from only the near-surface carriers, eliminating the possible complications from the diffusion into the bulk in the transmission measurements.

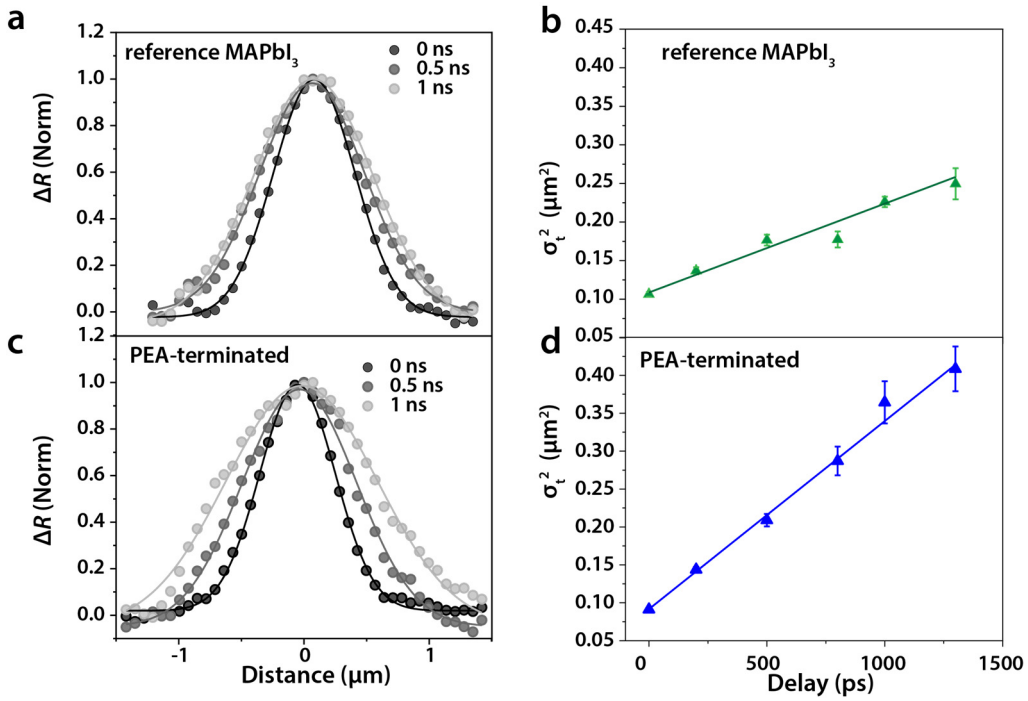

Figure 5. **Near-surface carrier diffusion (~25 nm probing depth) measured by transient reflection microscopy**. (a) 1D carrier population profiles in a reference $MAPbI_3$ microplate with the maximum ΔR signal normalized. (b) σ_t^2 plotted as a function of pump-probe delay time extracted from the data shown in (a). The solid line is the linear fit to calculate the diffusion constants. (c) 1D carrier population profiles in a PEA terminated $MAPbI_3$ microplate with the maximum ΔR signal normalized. (b) σ_t^2 plotted as a function of pump-probe delay time extracted from the data shown in (c). The solid line is the linear fit to calculate the diffusion constants. Pump photon energy = 1.77 eV, probe photon energy = 1.59 eV.

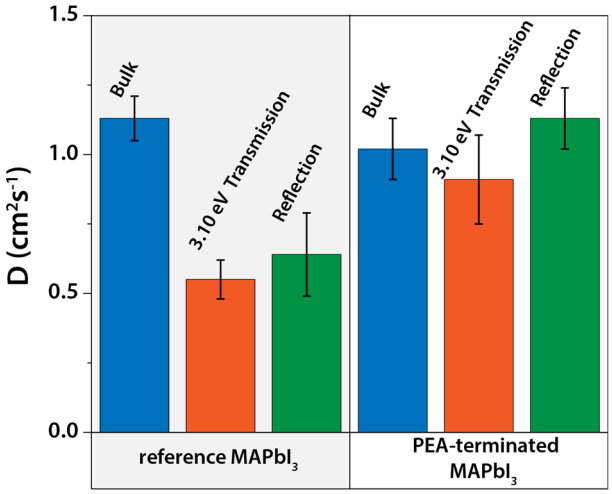

Figure 6. **Comparison of average bulk and near-surface carrier diffusion constants**. Diffusion constants measured in multiple reference microplates (4 for transmission mode and 4 for reflection modes) and PEA-terminated $MAPbI_3$ microplates (11 for transmission mode and 4 for reflection modes).

The results from a typical untreated reference $MAPbI_3$ crystal are shown in Figures 5a and 5b, with a *D* of 0.58 ± 0.04 cm^2s^{-1} for the carriers in the 25-nm near-surface region probed in the reflection mode. In comparison, the near-surface carrier diffusion constant in a PEA-terminated crystal is measured to be 1.24 ± 0.04 cm^2s^{-1} (Figures 5c and 5d), similar to the bulk value. These *D* values agree well with the results from the transmission mode TAM with a 3.10 eV pump, which further supports that PEA functionalization can improve near-surface carrier transport. Figure 6 summarizes the average bulk and near-surface carrier diffusion constants from multiple crystals imaged by transmission and reflection modes. The average diffusion constant for the bulk carriers is 1.13 ± 0.08 cm^2s^{-1} and 1.02 ± 0.11 cm^2s^{-1} in the reference and PEA-terminated microplates, respectively, in good agreements with other reports on single crystals of $MAPbI_3$.[63-65] In contrast, the average diffusion constant for the carriers in the subsurface region is improved from ~ 0.6 cm^2s^{-1} to ~ 1 cm^2s^{-1} by PEA surface functionalization.

Notably, the average *D* for the carriers in the 25-nm region probed by the reflection mode is similar to that of the carriers generated in the 40-nm depth by the 3.10 eV pump in the

transmission mode (Figure 6). If a significant portion of the carriers generated near the surface of the untreated crystals can diffuse into the bulk, one should expect a higher *D* in the transmission mode due to more contribution from the bulk carriers. However, this is not what we observed, which implies that the diffusion from the ~ 40 nm subsurface region into the bulk is not significant for the untreated crystals. The diffusion into the bulk can be hindered by factors such as such as surface recombination, trapping, or band bending.[26,27] While surface recombination generally occur within a few nm of the surface, band bending effects can extend much longer distance.[26,27] The suppression of carrier diffusion into the bulk in the untreated perovskite crystals is detrimental for the function of solar cells. However, this problem can be overcome with PEA functionalization, which facilitates the carriers to diffuse into the bulk (i.e. along the z direction). It is likely that the diffusion at the surface is much lower than the value we obtained in a slab of 10s of nm here. For example, exciton diffusion constant in $(BA)_2PbI_4$ (BA is butylammonium) has been reported to be 0.01- 0.06 cm^2s^{-1},[49,66] which could be viewed as a comparable system to the topmost surface layer of the untreated crystals. The exciton diffusion constant is much improved in $(PEA)_2PbI_4$, to ~ 0.2 cm^2s^{-1}.[49]

Discussion: The TAM results demonstrate that the near surface carrier transport properties in $MAPbI_3$ can be favorably improved by surface functionalization with PEA ligands. These results are consistent with a recent report[49] that showed almost one order of magnitude higher carrier diffusion coefficient in 2D perovskite $(PEA)_2PbI_4$ than that of $(BA)_2PbI_4$. One possible explanation is that that the scattering of carriers was reduced at or near the surface by the PEA ligands. For band-like transport in semiconductors, the diffusion constant is given by $D = \frac{\tau_s kT}{m}$, where τ_s is the momentum relaxation time corresponding to the inverse of the sum of all scattering rates, k is the Boltzmann constant, T is temperature, and m is the effective mass of the carriers.[24] The reduced

diffusivity near the surface region for the untreated microplates implies a shorter τ_s due to more frequent scattering events. These processes can include scattering of carriers by optical and acoustic phonons, structural defects, and impurities.[52,53] The surface defect density is reduced by one order of magnitude with PEA functionalization as revealed by the modeling of the carrier-density PL dynamics, which suppresses defect scattering and prolongs τ_s. Secondly, PEA ligands increase the structural rigidity of the perovskite lattice.[34] Theoretical calculations have suggested that stiffening of the inorganic Pb−I lattice leads to fewer low frequency optical phonon modes and reduces the frequency of electron−phonon scattering.[34,67] Thus, on the PEA-terminated surface, both structural disorder (such as defects) and dynamic disorder (electron-phonon scattering) are suppressed, leading to enhanced transport behaviors near the surfaces. In addition to reduced scattering, the PEA functionalization also eliminates the shallow energy trap states as indicated by the TA spectra in Figure 2b. The trap states can localize the free carriers to the near-surface region with a reduced effective diffusion constant D_{eff}, $D_{eff} = D_0 \frac{\tau_t}{\tau_t+\tau_f}$, where D_0 is the diffusion constant for the free carriers, τ_t is the average time carriers stay in the traps and τ_f is the time for the carriers to be released from the traps.[27]

Overall, PEA surface functionalization can lead to improved optoelectronic devices because of two key factors: the reduced surface trap density and the enhanced in-plane near-surface carrier diffusion. The elimination of surface traps is critical for allowing the carriers to diffuse into the bulk, which is necessary for the function of solar cells. The improvement in the near-surface diffusivity could be important for carrier transport across different crystalline domain as most perovskite solar cell devices are based on polycrystalline films with many domains of different orientations. Indeed, PEA functionalization has been demonstrated to improve the efficiency of polycrystalline perovskites solar cells.[35,36] In addition, another type of solar cell architecture based

on interdigitated back contact (IBC) has emerged.[68-71] In the IBC architecture the electron- and hole-selective electrodes are placed on the backside of the semiconductor layer in an interdigitated fashion, which requires lateral carrier diffusion. Finally, efficient lateral carrier transport between the electrodes is critical for the device performance of photodetectors.[72]

Conclusions

In summary, we demonstrated that the carrier transport near the surface of $MAPbI_3$ can be significantly improved by PEA ligand surface functionalization. By using ultrafast transient transmission and reflection microscopy, we were able to distinguish the surface-like and bulk-like carrier diffusion coefficients. Specifically, for the untreated $MAPbI_3$ crystals, the carrier diffusion coefficient for the 40-nm subsurface layer is only 55% of the bulk diffusion constant; with the PEA surface ligands, the surface carriers have similar diffusion constant as the bulk carriers of around 1 cm^2s^{-1}. In addition, the PEA functionalization reduces the surface defect density by more than one order of magnitude as revealed by the kinetic modeling of carrier-density-dependent lifetime measurements. These results suggest that PEA surface functionalization is effective in reducing both structural defects and electron-phonon scattering at the surface and provide fundamental insights on how to design new methods to improve the surface properties of hybrid perovskite materials for high performance optoelectronic devices, such as solar cells and photodetectors.

Methods:

Synthesis of single-crystal perovskite microplates

The reference $MAPbI_3$ microplates were synthesized by immersing a piece of $PbAc_2$ coated glass slide in a solution of MAI in isopropanol (IPA) at room temperature, with the $PbAc_2$ coated side facing up.[37] The $PbAc_2$ thin film was prepared by dropcasting 100 mg/mL $PbAc_2 \cdot 3H_2O$ aqueous

solution on a glass slide. The coated substrate was then annealed at 50 °C in an oven before it was dipped into 1 mL precursor solution in a reaction vial. The PEA-terminated $MAPbI_3$ microplates studied herein were synthesized by immersing a piece of $PbAc_2$ coated glass slide in a mixed solution of MAI and PEAI in IPA at room temperature, with the $PbAc_2$ coated side facing up. The precursor solution was made by mixing solutions of PEAI (40 mg/mL) and MAI (40 mg/mL) in IPA with a volume ratio of 0.45/0.55 (the corresponding molar ratio of PEA to MA is 0.52). After a reaction time of ~3 days, the glass slide was taken out, washed in IPA and dried under N_2 flow. Note that both of these syntheses also produced some nanowire by-products but they can be easily avoided for the single object studies here. In additional, the films of PEA-terminated $MAPbI_3$ sample have more tendency to peel off from the glass slides than the reference $MAPbI_3$ microplates. Other growth conditions that led to mixed 2D/3D halide perovskite products are discussed in the Supporting Information.

Optical absorption and photoluminescence (PL) measurements

A home-built microscope was used for the micro-absorption and PL spectroscopy measurements.[66] For the micro-absorption measurements, a halogen tungsten lamp was used as white light source which was focused by an objective (20×, NA = 0.45, Olympus) to spot with size of ~2 μm on the sample. The transmitted light was collected by anther objective (40×, NA = 0.6, Nikon), and detected by a spectrometer (Andor Shamrock 303i) and CCD (Andor Newton 920). The same spectrometer and CCD combination were used for PL spectroscopy. A picosecond pulse laser with wavelength of 447 nm was used as the excitation light and an objective (40×, NA = 0.6, Nikon) was employed to focus the excitation light on the sample and collect the scattered PL light in wide-filed mode. For the PL decay dynamics, the collected light was guided to a single photon avalanche diode (PicoQuant, PDM series) with a single photon counting module (PicoQuant). In order to

exclude diffusion from the PL decays, the home-built setup is not a strict confocal such that emission beyond the excitation spot is also collected. As obtained dynamics were fitted with biexponential decay convoluted with instrumental response function as given by,

$$I(t) = conv(\exp\left(-\frac{t^2}{w^2}\right), \Theta(t_0) \cdot (A_1 \cdot \exp\left(-\frac{t}{\tau_1}\right) + A_2 \cdot \exp\left(-\frac{t}{\tau_2}\right)))$$

where I is the PL intensity as a function time t, Θ is a step function, t_0 is time zero, τ_1 and τ_2 are time constants for the exponential decay, A_1 and A_2 are amplitudes of the two decays, w describe the instrumental response. The time resolution of the system is around 100 ps.

Transient absorption microscopy (TAM)

The details of the home-built TAM setup (Figure S13) were described in our previous publication.[57] The same setup was used for the $MAPbI_3$ microplates measurements in this work. Briefly, the output from two independent optical parametric amplifiers (OPAs, 750 kHz, 200~300 fs, Light Conversion) served as the pump and probe beam respectively. Both the pump and probe beams were focused on the sample with an oil objective (60 ×, NA = 1.49, Nikon). To improve the signal to noise ratio, an acousto-optic modulator (Gooch and Housego, R23080-1) was used to modulate the pump beam at 100 kHz. A mechanical translation stage (Thorlabs, DDS600-E) was used to delay the probe with respect to the pump. For the diffusion images, a 2D galvo mirror (Thorlabs GVS012) was employed to scan the probe beam relative to the pump beam in space at multiple delay times. Spatial filters were used to optimize the profile of the beams. The transmitted or reflected probe light was detected by an avalanche photodiode (APD) (Hamamatsu, C5331-04), and the pump-induced change in probe transmission (ΔT) or reflection (ΔR) was extracted by a lock-in amplifier (SR830, SRS Inc.)

Acknowledgments

The optical spectroscopy and microscopy work at Purdue are supported by U.S. Department of Energy, Office of Basic Energy Sciences through award DE-SC0016356. The synthesis and structural characterizations of the (surface functionalized) perovskites at University of Wisconsin – Madison are supported by the U.S. Department of Energy, Office of Basic Energy Sciences, Division of Materials Sciences and Engineering, under award DE-FG02-09ER46664.

Supporting Information

Supporting Information Available: additional discussion on the crystal growth, crystallographic data, optical and SEM images, PL and micro-absorption spectra, details on the fitting of PL dynamics, TAM experimental setup, and additional TAM images and dynamics. This material is available free of charge via the Internet at http://pubs.acs.org.

AUTHOR INFORMATION

Ti Wang, Yongping Fu, and Linrui Jin contributed equally to this work.

Corresponding Authors

*E-mail: libai-huang@purdue.edu, jin@chem.wisc.edu

References

(1) Lee, M. M.; Teuscher, J.; Miyasaka, T.; Murakami, T. N.; Snaith, H. J. Efficient hybrid solar cells based on meso-superstructured organometal halide perovskites. *Science* **2012**, 1228604.
(2) Burschka, J.; Pellet, N.; Moon, S.-J.; Humphry-Baker, R.; Gao, P.; Nazeeruddin, M. K.; Grätzel, M. Sequential deposition as a route to high-performance perovskite-sensitized solar cells. *Nature* **2013**, *499*, 316.
(3) Shi, D.; Adinolfi, V.; Comin, R.; Yuan, M.; Alarousu, E.; Buin, A.; Chen, Y.; Hoogland, S.; Rothenberger, A.; Katsiev, K.; Losovyj, Y.; Zhang, X.; Dowben, P. A.; Mohammed, O. F.; Sargent, E. H.; Bakr, O. M. Low trap-state density and long carrier diffusion in organolead trihalide perovskite single crystals. *Science* **2015**, *347*, 519.

(4) Jeon, N. J.; Noh, J. H.; Yang, W. S.; Kim, Y. C.; Ryu, S.; Seo, J.; Seok, S. I. Compositional engineering of perovskite materials for high-performance solar cells. *Nature* **2015**, *517*, 476.
(5) Zhu, H.; Fu, Y.; Meng, F.; Wu, X.; Gong, Z.; Ding, Q.; Gustafsson, M. V.; Trinh, M. T.; Jin, S.; Zhu, X. Lead halide perovskite nanowire lasers with low lasing thresholds and high quality factors. *Nat. Mater.* **2015**, *14*, 636-642.
(6) Fang, Y.; Dong, Q.; Shao, Y.; Yuan, Y.; Huang, J. Highly narrowband perovskite single-crystal photodetectors enabled by surface-charge recombination. *Nat. Photonics* **2015**, *9*, 679-686.
(7) Lin, K.; Xing, J.; Quan, L. N.; de Arquer, F. P. G.; Gong, X.; Lu, J.; Xie, L.; Zhao, W.; Zhang, D.; Yan, C.; Li, W.; Liu, X.; Lu, Y.; Kirman, J.; Sargent, E. H.; Xiong, Q.; Wei, Z. Perovskite light-emitting diodes with external quantum efficiency exceeding 20 per cent. *Nature* **2018**, *562*, 245-248.
(8) Fu, Y.; Zhu, H.; Chen, J.; Hautzinger, M. P.; Zhu, X. Y.; Jin, S. Metal halide perovskite nanostructures for optoelectronic applications and the study of physical properties. *Nature Reviews Materials* **2019**, *4*, 169-188.
(9) Seker, F.; Meeker, K.; Thomas F Kuech, a.; Ellis, A. B. Surface Chemistry of Prototypical Bulk II−VI and III−V Semiconductors and Implications for Chemical Sensing. *Chem. Rev.* **2000**, *100*, 2505-2536.
(10) Ashkenasy, G.; Cahen, D.; Cohen, R.; Abraham Shanzer, a.; Vilan, A. Molecular Engineering of Semiconductor Surfaces and Devices. *Acc. Chem. Res.* **2002**, *35*, 121-128.
(11) Wong, K. T.; Lewis, N. S. What a Difference a Bond Makes: The Structural, Chemical, and Physical Properties of Methyl-Terminated Si(111) Surfaces. *Acc. Chem. Res.* **2014**, *47*, 3037-3044.
(12) Schulz, P.; Cahen, D.; Kahn, A. Halide Perovskites: Is It All about the Interfaces? *Chem Rev* **2019**, *119*, 3349-3417.
(13) Yang, S.; Wang, Y.; Liu, P.; Cheng, Y.-B.; Zhao, H. J.; Yang, H. G. Functionalization of perovskite thin films with moisture-tolerant molecules. *Nat. Energy* **2016**, *1*, 1-7.
(14) Zheng, X.; Chen, B.; Dai, J.; Fang, Y.; Bai, Y.; Lin, Y.; Wei, H.; Zeng, X. C.; Huang, J. Defect passivation in hybrid perovskite solar cells using quaternary ammonium halide anions and cations. *Nat. Energy* **2017**, *2*, 17102.
(15) Braly, I. L.; deQuilettes, D. W.; Pazos-Outón, L. M.; Burke, S.; Ziffer, M. E.; Ginger, D. S.; Hillhouse, H. W. Hybrid perovskite films approaching the radiative limit with over 90% photoluminescence quantum efficiency. *Nat. Photonics* **2018**, *12*, 355-361.
(16) Wang, R.; Xue, J.; Wang, K.-L.; Wang, Z. K.; Luo, Y.; Fenning, D.; Xu, G.; Nuryyeva, S.; Huang, T.; Zhao, Y.; Yang, J. L.; Zhu, J.; Wang, M.; Tan, S.; Yavuz, I.; Houk, K. N.; Yang, Y. Constructive molecular configurations for surface-defect passivation of perovskite photovoltaics. *Science* **2019**, *366*, 1509-1513.
(17) Xu, W.; Hu, Q.; Bai, S.; Bao, C.; Miao, Y.; Yuan, Z.; Borzda, T.; Barker, A. J.; Tyukalova, E.; Hu, Z.; Kawecki, M.; Wang, H.; Yan, Z.; Liu, X.; Shi, X.; Uvdal, K.; Fahlman, M.; Zhang, W.; Duchamp, M.; Liu, J.-M.; Petrozza, A.; Wang, J.; Liu, L.-M.; Huang, W.; Gao, F. Rational molecular passivation for high-performance perovskite light-emitting diodes. *Nat. Photonics* **2019**, *13*, 418-424.
(18) Nenon, D. P.; Pressler, K.; Kang, J.; Koscher, B. A.; Olshansky, J. H.; Osowiecki, W. T.; Koc, M. A.; Wang, L.-W.; Alivisatos, A. P. Design Principles for Trap-Free CsPbX3 Nanocrystals: Enumerating and Eliminating Surface Halide Vacancies with Softer Lewis Bases. *J. Am. Chem. Soc.* **2018**, *140*, 17760-17772.

(19) de Quilettes, D. W.; Vorpahl, S. M.; Stranks, S. D.; Nagaoka, H.; Eperon, G. E.; Ziffer, M. E.; Snaith, H. J.; Ginger, D. S. Impact of microstructure on local carrier lifetime in perovskite solar cells. *Science* **2015**, *348*, 683-686.
(20) Bischak, C. G.; Sanehira, E. M.; Precht, J. T.; Luther, J. M.; Ginsberg, N. S. Heterogeneous Charge Carrier Dynamics in Organic–Inorganic Hybrid Materials: Nanoscale Lateral and Depth-Dependent Variation of Recombination Rates in Methylammonium Lead Halide Perovskite Thin Films. *Nano Lett.* **2015**, *15*, 4799-4807.
(21) Stewart, R. J.; Grieco, C.; Larsen, A. V.; Maier, J. J.; Asbury, J. B. Approaching Bulk Carrier Dynamics in Organo-Halide Perovskite Nanocrystalline Films by Surface Passivation. *J. Phys. Chem. Lett.* **2016**, *7*, 1148-1153.
(22) Yang, Y.; Yang, M.; Moore, D. T.; Yan, Y.; Miller, E. M.; Zhu, K.; Beard, M. C. Top and bottom surfaces limit carrier lifetime in lead iodide perovskite films. *Nat. Energy* **2017**, *2*, 16207.
(23) Bonabi Naghadeh, S.; Luo, B.; Abdelmageed, G.; Pu, Y.-C.; Zhang, C.; Zhang, J. Z. Photophysical Properties and Improved Stability of Organic–Inorganic Perovskite by Surface Passivation. *J. Phys. Chem. C* **2018**, *122*, 15799-15818.
(24) Sze, S. M.; Ng, K. K. *Physics of semiconductor devices*; John Wiley & Sons, 2006.
(25) Tanaka, T.; Harata, A.; Sawada, T. Subpicosecond surface-restricted carrier and thermal dynamics by transient reflectivity measurements. *J. Appl. Phys.* **1998**, *82*, 4033-4038.
(26) Li, C. M.; Sjodin, T.; Ying, Z. C.; Dai, H. L. Photoexcited carrier diffusion near a Si(111) surface and in the Si bulk. *Appl. Surf. Sci.* **1996**, *104-105*, 57-60.
(27) Qi, J.; Angerer, W.; Yeganeh, M. S.; Yodh, A. G.; Theis, W. M. Transverse diffusion of minority carriers confined near the GaAs surface plane. *Phys. Rev. B* **1995**, *51*, 13533-13537.
(28) Saparov, B.; Mitzi, D. B. Organic–Inorganic Perovskites: Structural Versatility for Functional Materials Design. *Chem. Rev.* **2016**, *116*, 4558-4596.
(29) Mao, L.; Stoumpos, C. C.; Kanatzidis, M. G. Two-Dimensional Hybrid Halide Perovskites: Principles and Promises. *J Am Chem Soc* **2019**, *141*, 1171-1190.
(30) Dou, L.; Wong, A. B.; Yu, Y.; Lai, M.; Kornienko, N.; Eaton, S. W.; Fu, A.; Bischak, C. G.; Ma, J.; Ding, T.; Ginsberg, N. S.; Wang, L. W.; Alivisatos, A. P.; Yang, P. Atomically thin two-dimensional organic-inorganic hybrid perovskites. *Science* **2015**, *349*, 1518-1521.
(31) Kawano, N.; Koshimizu, M.; Sun, Y.; Yahaba, N.; Fujimoto, Y.; Yanagida, T.; Asai, K. Effects of Organic Moieties on Luminescence Properties of Organic–Inorganic Layered Perovskite-Type Compounds. *J. Phys. Chem. C* **2014**, *118*, 9101-9106.
(32) Qi, Z.; Leiqiang, C.; Feng, Z.; Wei, J.; Goki, E. Excitonic Properties of Chemically Synthesized 2D Organic–Inorganic Hybrid Perovskite Nanosheets. *Adv. Mater.* **2018**, *30*, 1704055.
(33) Ni, L.; Huynh, U.; Cheminal, A.; Thomas, T. H.; Shivanna, R.; Hinrichsen, T. F.; Ahmad, S.; Sadhanala, A.; Rao, A. Real-Time Observation of Exciton–Phonon Coupling Dynamics in Self-Assembled Hybrid Perovskite Quantum Wells. *ACS Nano* **2017**, *11*, 10834-10843.
(34) Gong, X.; Voznyy, O.; Jain, A.; Liu, W.; Sabatini, R.; Piontkowski, Z.; Walters, G.; Bappi, G.; Nokhrin, S.; Bushuyev, O.; Yuan, M.; Comin, R.; McCamant, D.; Kelley, S. O.; Sargent, E. H. Electron–phonon interaction in efficient perovskite blue emitters. *Nat. Mater.* **2018**, *17*, 550-556.
(35) Wang, Y.; Zhang, T.; Kan, M.; Li, Y.; Wang, T.; Zhao, Y. Efficient α-CsPbI3 Photovoltaics with Surface Terminated Organic Cations. *Joule* **2018**, *2*, 2065-2075.
(36) Jiang, Q.; Zhao, Y.; Zhang, X.; Yang, X.; Chen, Y.; Chu, Z.; Ye, Q.; Li, X.; Yin, Z.; You, J. Surface passivation of perovskite film for efficient solar cells. *Nat. Photonics* **2019**, *13*, 460-466.
(37) Fu, Y.; Meng, F.; Rowley, M. B.; Thompson, B. J.; Shearer, M. J.; Ma, D.; Hamers, R. J.; Wright, J. C.; Jin, S. Solution Growth of Single Crystal Methylammonium Lead Halide Perovskite

Nanostructures for Optoelectronic and Photovoltaic Applications. *J. Am. Chem. Soc.* **2015**, *137*, 5810-5818.
(38) Chen, Z.; Dong, Q.; Liu, Y.; Bao, C.; Fang, Y.; Lin, Y.; Tang, S.; Wang, Q.; Xiao, X.; Bai, Y.; Deng, Y.; Huang, J. Thin single crystal perovskite solar cells to harvest below-bandgap light absorption. *Nat. Commun.* **2017**, *8*, 1-7.
(39) Murali, B.; Kolli, H. K.; Yin, J.; Ketavath, R.; Bakr, O. M.; Mohammed, O. F. Single Crystals: The Next Big Wave of Perovskite Optoelectronics. *ACS Materials Letters* **2020**, *2*, 184-214.
(40) Zhu, T.; Snaider, J. M.; Yuan, L.; Huang, L. Ultrafast Dynamic Microscopy of Carrier and Exciton Transport. *Annu. Rev. Phys. Chem.* **2019**, *70*, 219-244.
(41) Draguta, S.; Thakur, S.; Morozov, Y. V.; Wang, Y.; Manser, J. S.; Kamat, P. V.; Kuno, M. Spatially Non-uniform Trap State Densities in Solution-Processed Hybrid Perovskite Thin Films. *J. Phys. Chem. Lett.* **2016**, *7*, 715-721.
(42) deQuilettes, D. W.; Jariwala, S.; Burke, S.; Ziffer, M. E.; Wang, J. T. W.; Snaith, H. J.; Ginger, D. S. Tracking Photoexcited Carriers in Hybrid Perovskite Semiconductors: Trap-Dominated Spatial Heterogeneity and Diffusion. *ACS Nano* **2017**, *11*, 11488-11496.
(43) Snaider, J. M.; Guo, Z.; Wang, T.; Yang, M.; Yuan, L.; Zhu, K.; Huang, L. Ultrafast Imaging of Carrier Transport across Grain Boundaries in Hybrid Perovskite Thin Films. *ACS Energy Lett* **2018**, *3*, 1402-1408.
(44) Delor, M.; Weaver, H. L.; Yu, Q.; Ginsberg, N. S. Imaging material functionality through three-dimensional nanoscale tracking of energy flow. *Nat. Mater.* **2020**, *19*, 56-62.
(45) Geng, W.; Tong, C.-J.; Tang, Z.-K.; Yam, C.; Zhang, Y.-N.; Lau, W.-M.; Liu, L.-M. Effect of surface composition on electronic properties of methylammonium lead iodide perovskite. *Journal of Materiomics* **2015**, *1*, 213-220.
(46) Quarti, C.; De Angelis, F.; Beljonne, D. Influence of Surface Termination on the Energy Level Alignment at the $CH_3NH_3PbI_3$ Perovskite/C_{60} Interface. *Chem. Mater.* **2017**, *29*, 958-968.
(47) She, L.; Liu, M.; Zhong, D. Atomic Structures of $CH_3NH_3PbI_3$ (001) Surfaces. *ACS Nano* **2016**, *10*, 1126-1131.
(48) Komesu, T.; Huang, X.; Paudel, T. R.; Losovyj, Y. B.; Zhang, X.; Schwier, E. F.; Kojima, Y.; Zheng, M.; Iwasawa, H.; Shimada, K.; Saidaminov, M. I.; Shi, D.; Abdelhady, A. L.; Bakr, O. M.; Dong, S.; Tsymbal, E. Y.; Dowben, P. A. Surface Electronic Structure of Hybrid Organo Lead Bromide Perovskite Single Crystals. *J. Phys. Chem. C* **2016**, *120*, 21710-21715.
(49) Seitz, M.; Magdaleno, A. J.; Alcazar-Cano, N.; Melendez, M.; Lubbers, T. J.; Walraven, S. W.; Pakdel, S.; Prada, E.; Delgado-Buscalioni, R.; Prins, F. Exciton diffusion in two-dimensional metal-halide perovskites. *Nat Commun* **2020**, *11*, 2035.
(50) Spitha, N.; Kohler, D. D.; Hautzinger, M. P.; Li, J.; Jin, S.; Wright, J. C. Discerning between Exciton and Free-Carrier Behaviors in Ruddlesden–Popper Perovskite Quantum Wells through Kinetic Modeling of Photoluminescence Dynamics. *J. Phys. Chem. C* **2020**, *124*, 17430-17439.
(51) Fu, Y.; Wu, T.; Wang, J.; Zhai, J.; Shearer, M. J.; Zhao, Y.; Hamers, R. J.; Kan, E.; Deng, K.; Zhu, X. Y.; Jin, S. Stabilization of the Metastable Lead Iodide Perovskite Phase via Surface Functionalization. *Nano Lett.* **2017**, *17*, 4405-4414.
(52) Fu, Y.; Zheng, W.; Wang, X.; Hautzinger, M. P.; Pan, D.; Dang, L.; Wright, J. C.; Pan, A.; Jin, S. Multicolor Heterostructures of Two-Dimensional Layered Halide Perovskites that Show Interlayer Energy Transfer. *J. Am. Chem. Soc.* **2018**, *140*, 15675-15683.
(53) Wang, W.; Banerjee, S.; Jia, S.; Steigerwald, M. L.; Herman, I. P. Ligand Control of Growth, Morphology, and Capping Structure of Colloidal CdSe Nanorods. *Chem. Mater.* **2007**, *19*, 2573-2580.

(54) Blancon, J. C.; Stier, A. V.; Tsai, H.; Nie, W.; Stoumpos, C. C.; Traoré, B.; Pedesseau, L.; Kepenekian, M.; Katsutani, F.; Noe, G. T.; Kono, J.; Tretiak, S.; Crooker, S. A.; Katan, C.; Kanatzidis, M. G.; Crochet, J. J.; Even, J.; Mohite, A. D. Scaling law for excitons in 2D perovskite quantum wells. *Nat. Commun.* **2018**, *9*, 2254.
(55) Liu, J.; Leng, J.; Wu, K.; Zhang, J.; Jin, S. Observation of Internal Photoinduced Electron and Hole Separation in Hybrid Two-Dimentional Perovskite Films. *J. Am. Chem. Soc.* **2017**, *139*, 1432-1435.
(56) Stranks, S. D.; Burlakov, V. M.; Leijtens, T.; Ball, J. M.; Goriely, A.; Snaith, H. J. Recombination Kinetics in Organic-Inorganic Perovskites: Excitons, Free Charge, and Subgap States. *Phys. Rev. Applied* **2014**, *2*, 034007.
(57) Guo, Z.; Wan, Y.; Yang, M.; Snaider, J.; Zhu, K.; Huang, L. Long-range hot-carrier transport in hybrid perovskites visualized by ultrafast microscopy. *Science* **2017**, *356*, 59-62.
(58) Giorgi, G.; Fujisawa, J.-I.; Segawa, H.; Yamashita, K. Small Photocarrier Effective Masses Featuring Ambipolar Transport in Methylammonium Lead Iodide Perovskite: A Density Functional Analysis. *J. Phys. Chem. Lett.* **2013**, *4*, 4213-4216.
(59) Chang, A. Y.; Cho, Y. J.; Chen, K. C.; Chen, C. W.; Kinaci, A.; Diroll, B. T.; Wagner, M. J.; Chan, M. K.; Lin, H. W.; Schaller, R. D. Slow organic-to-inorganic sub-lattice thermalization in methylammonium lead halide perovskites observed by ultrafast photoluminescence. *Adv. Energy Mater.* **2016**, *6*, 1600422.
(60) Yang, Y.; Ostrowski, D. P.; France, R. M.; Zhu, K.; Van De Lagemaat, J.; Luther, J. M.; Beard, M. C. Observation of a hot-phonon bottleneck in lead-iodide perovskites. *Nat. Photonics* **2016**, *10*, 53-59.
(61) Fu, J.; Xu, Q.; Han, G.; Wu, B.; Huan, C. H. A.; Leek, M. L.; Sum, T. C. Hot carrier cooling mechanisms in halide perovskites. *Nat. Commun.* **2017**, *8*, 1300.
(62) van Driel, H. M. Kinetics of high-density plasmas generated in Si by 1.06- and 0.53- microm picosecond laser pulses. *Phys Rev B Condens Matter* **1987**, *35*, 8166-8176.
(63) Tian, W.; Zhao, C.; Leng, J.; Cui, R.; Jin, S. Visualizing Carrier Diffusion in Individual Single-Crystal Organolead Halide Perovskite Nanowires and Nanoplates. *J. Am. Chem. Soc.* **2015**, *137*, 12458-12461.
(64) Guo, Z.; Zhou, N.; Williams, O. F.; Hu, J.; You, W.; Moran, A. M. Imaging Carrier Diffusion in Perovskites with a Diffractive Optic-Based Transient Absorption Microscope. *J. Phys. Chem. C* **2018**, *122*, 10650-10656.
(65) Hill, A. H.; Kennedy, C. L.; Massaro, E. S.; Grumstrup, E. M. Perovskite Carrier Transport: Disentangling the Impacts of Effective Mass and Scattering Time Through Microscopic Optical Detection. *J Phys Chem Lett* **2018**.
(66) Deng, S.; Shi, E.; Yuan, L.; Jin, L.; Dou, L.; Huang, L. Long-range exciton transport and slow annihilation in two-dimensional hybrid perovskites. *Nat. Commun.* **2020**, *11*, 1-8.
(67) He, J.; Fang, W.-H.; Long, R.; Prezhdo, O. V. Increased Lattice Stiffness Suppresses Nonradiative Charge Recombination in MAPbI 3Doped with Larger Cations: Time-Domain Ab Initio Analysis. *ACS Energy Lett.* **2018**, *3*, 2070-2076.
(68) Jumabekov, A. N.; Della Gaspera, E.; Xu, Z. Q.; Chesman, A. S. R.; van Embden, J.; Bonke, S. A.; Bao, Q.; Vak, D.; Bach, U. Back-contacted hybrid organic–inorganic perovskite solar cells. *J. Mater. Chem. C* **2016**, *4*, 3125-3130.
(69) Wong-Stringer, M.; Routledge, T. J.; McArdle, T.; Wood, C. J.; Game, O. S.; Smith, J. A.; Bishop, J. E.; Vaenas, N.; Coles, D. M.; Buckley, A. R.; Lidzey, D. G. A flexible back-contact perovskite solar micro-module. *Energy Environ. Sci.* **2019**, *12*, 1928-1937.

(70) Tainter, G. D.; Hörantner, M. T.; Pazos-Outón, L. M.; Lamboll, R. D.; Āboliņš, H.; Leijtens, T.; Mahesh, S.; Friend, R. H.; Snaith, H. J.; Joyce, H. J.; Deschler, F. Long-Range Charge Extraction in Back-Contact Perovskite Architectures via Suppressed Recombination. *Joule* **2019**, *3*, 1301-1313.
(71) Song, Y.; Bi, W.; Wang, A.; Liu, X.; Kang, Y.; Dong, Q. Efficient lateral-structure perovskite single crystal solar cells with high operational stability. *Nat. Commun.* **2020**, *11*, 274.
(72) Hu, X.; Zhang, X.; Liang, L.; Bao, J.; Li, S.; Yang, W.; Xie, Y. High-Performance Flexible Broadband Photodetector Based on Organolead Halide Perovskite. *Adv. Funct. Mater.* **2014**, *24*, 7373-7380.